First-principles investigation of Sc-III/IV under high pressure

Sheng-Cai Zhu,[1] Xiao-Zhi Yan,[2] Scott Fredericks,[1] Yan-Ling Li,[3,*] and Qiang Zhu[1,†]

[1]*Department of Physics and Astronomy, High Pressure Science and Engineering Center, University of Nevada, Las Vegas, Nevada 89154, USA*
[2]*Academy for Advanced Interdisciplinary Studies and Department of Physics,*
Southern University of Science and Technology, Shenzhen 518055, China
[3]*School of Physics and Electronic Engineering, Laboratory for Quantum Design of Functional Materials,*
Jiangsu Normal University, Xuzhou 221116, China

Using an *ab initio* evolutionary structure prediction method in conjunction with density functional theory, we performed a systematic investigation of the structural transition of elemental scandium under pressure up to 250 GPa. Our prediction successfully reproduced several allotropes which have been reported in the literature, including the Sc-I, Sc-II, and Sc-V. Moreover, we observed a series of energetically degenerate and geometrically similar structures at 110–195 GPa, which can partly explain the experimental observations regarding the unsolved phases III and IV reported by Y. Akahama *et al.* [Phys. Rev. Lett. **94**, 195503 (2005)]. A detailed comparison of the powder x-ray diffraction pattern suggested that the $Ccca$-20 phase is a likely candidate for the observed Sc-III, while Sc-IV may be explained by a structure with random stacking of two different structural units. We also used the candidate Sc-III structure as the model system to explore its superconducting behavior under pressures between 80 and 130 GPa. The predicted superconducting transition temperature T_c values are in satisfactory agreement with previous experimental results.

I. INTRODUCTION

Elemental solids are the most fundamental cases for scientific studies on materials [1–5]. External pressure can effectively squeeze the crystal packing, alter the electronic configuration, and thus trigger the phase transition. Knowing the atomic structures is the key to understanding their properties under high pressure [1]. Searching for new allotropes under high pressure has been a long-term interest for scientists [6–8]. To date, many new structures and intriguing properties have been discovered under high pressure. For example, some simple metals, such as Li [9–13] and Na [14–16], transform to semimetallic, semiconducting, and even insulating phases under high pressure [17].

Sc, as the first $3d$ transition-metal, has attracted special interest [18–21]. In the past, scandium was often grouped with the rare-earth metals in the IIIB group since its mechanical, physical, and chemical properties are similar to those of Y, La, Pr, Nd, etc. [22]. Previous studies showed that group IIIB metals exhibit successive pressure-induced phase transitions [18,23–26] due to the electron transfer known as $s \rightarrow d$ transition under pressure [27–30]. These phase transitions follow a systematic sequence of hcp $\rightarrow$ Sm-type structure $\rightarrow$ double hcp (dhcp) $\rightarrow$ fcc $\rightarrow$ double fcc (dfcc) [18,31,32]. Sc was suggested to follow the same series of phase transitions under pressure as that found in Y and La [33,34]. However, two recent high-quality powder x-ray diffraction (PXRD) studies showed that the first high-pressure structure of Sc, known as

Sc-II, which is stable between 23 and 104 GPa, adopts an incommensurate structure (IC) consisting of two interpenetrating sublattices along the crystallographic c axis [35,36], making Sc distinct from other group IIIB metals [35,37]. Sc-II also provides an example of IC structure observed in non-main-group elements [38]. The intriguing structural complexity has stimulated a series of experimental and theoretical works on scandium [19,34,39–41].

Experimentally, Sc was found to exhibit resistant anomalies at about 17 GPa [42], and it becomes a superconductor at 20 GPa. The superconducting transition temperature T_c rapidly soars up with the increase in the external pressure [33,43]. Recently, it was found that the T_c in scandium reaches the highest value of 19.7 K at 107 GPa and then drops to about 8 K under further compression [18]. The sudden drop of T_c at 107 GPa is believed to be triggered by the structural phase transition. Using the monochromatic synchrotron PXRD technique, Sc was found to undergo four stages of structural transitions, i.e., Sc-I ($P6_3/mmc$) $\rightarrow$ Sc-II [$I4/mcm(00\gamma)$] $\rightarrow$ Sc-III (unsolved) $\rightarrow$ Sc-IV (unsolved) $\rightarrow$ Sc-V ($P6_122$), at around 23, 104, 140, and 240 GPa [37,44], respectively (see Fig. 1). Unfortunately, two structures (Sc-III and Sc-IV) are still unclear [45]. As Akahama *et al.* reported [37], these structures may contain a large number of atoms in the unit cell, according to the observed complex PXRD profiles. Due to the lack of atomic models of Sc-III and IV, the electron-phonon coupling (EPC) characteristic of Sc at high pressure beyond 107 GPa is still a mystery.

Here, we explore the high-pressure effects on Sc by using the *ab initio* evolutionary structure prediction method USPEX [46,47]. Through an extensive crystal structure search, we found a series of structures which are both energetically and
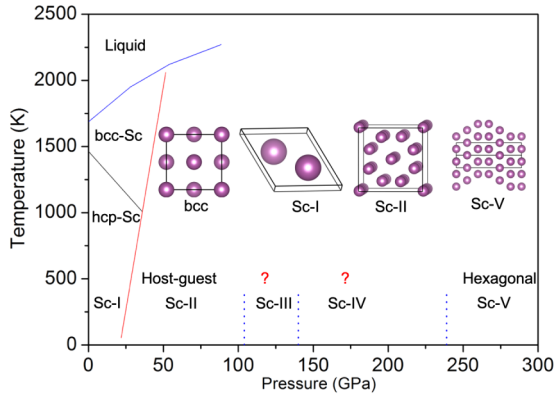
*ylli@jsnu.edu.cn
†qiang.zhu@unlv.edu

FIG. 1. The pressure-temperature phase diagram of scandium reproduced from the literature [37,40]. The inset shows the atomic structures of bcc, hcp (Sc-I), host-guest (Sc-II), and hexagonal (Sc-V), except Sc-III and Sc-IV.

geometrically degenerate at 110–195 GPa. Interestingly, all these structures possess two types of atoms: (1) one builds the layered distorted-hexagon framework; (2) the other can be explained as the intercalated atoms between the distorted-hexagon layers. By comparing the simulated PXRD profiles with previous experiment data, we suggest the $Ccca$-20 (No. 68) structure (ground state at pressures between 75 and 160 GPa) as the candidate model for Sc-III, while Sc-IV may be explained by random stacking of two structural units rather than the ground-state $Cmca$-32 (No. 64) structure at pressures between 160 and 195 GPa. We also used the candidate Sc-III structure as the model system to explore its superconducting behavior. The predicted pressure dependence of T_c is in satisfactory agreement with previous experimental results [18].

II. COMPUTATIONAL METHODS

Based on the evolutionary structure prediction method USPEX code [46,47] in conjunction with first-principles calculations, we performed several runs at 0, 30, 110, 150, 180, and 250 GPa with no more than 32 atoms in the unit cell. During the structure search, the first generation of structures was created randomly, the worst structures (40%) were discarded, and the best structures from each generation were kept. The next generations were created by heredity, mutation, and random-generator operations. Structure optimization evolved over a maximum of 40 generations. Each structure was optimized at the level of density functional theory (DFT) as implemented in the VASP code [48]. The exchange-correlation functional was described by the generalized gradient approximation in the Perdew-Burke-Ernzerhof parametrization [49], and the energy cutoff of the plane wave was set to 1000 eV. The geometry convergence criterion was set to 0.001 eV/Å for the maximal component of force and 0.01 GPa for stress. The Brillouin zone (BZ) was sampled by uniform Γ-centered meshes with a reciprocal space resolution of $2\pi \times 0.03\,\text{Å}^{-1}$. In order to check the dynamical stability of the candidate structures, we also carried out phonon calculations with the finite displacement method as implemented in the PHONOPY code [50].

To explore the superconducting properties of the selected structures, we calculated their electron-phonon coupling by using the QUANTUM ESPRESSO package [51] based on the projected augmented-wave potentials with cutoff energies of 100 and 800 Ry for the wave functions and the charge density, respectively. The electronic band structure and density of states were computed with a $24 \times 24 \times 24$ Monkhorst-Pack mesh. The electronic BZ integration in the phonon calculation was based on a $16 \times 16 \times 16$ Monkhorst-Pack k-point mesh. The dynamic matrix was computed based on a $4 \times 4 \times 4$ mesh of phonon wave vectors. The electron-phonon coupling was convergent with a finer grid of $24 \times 24 \times 24$ k points and a Gaussian smearing of 0.01 Ry.

III. RESULTS AND DISCUSSIONS

A. The phase diagram of Sc as a function of pressure

First, we found the hcp structure ($P6_3/mmc$, No. 194) is the stablest structure at 0 GPa, and the $I4/mcm$ (No. 108) structure is the ground state at 30 GPa. In the predicted Sc-II structure the lattice parameters at 30 GPa are $a = b = 7.3947\,\text{Å}$, $c = 10.2015\,\text{Å}$ with 32 atoms in the unit cell. The corresponding ratio γ between the c vector lengths in the host ($c1$) and guest ($c2$) lattices is 1.5, which is consistent with the results of Fujihisa *et al.* [36]. Such a γ value is believed to be the simplest approximate of the IC model of Sc-II. In principle, one may find a more complex structure with lower energy in a ratio closer to the real γ. However, such a model needs a much larger unit cell, and the search for the optimum γ value is beyond the scope of our work. Nevertheless, the agreement between theory and experiment encouraged us to explore the high-pressure effects further. At 110 GPa, our simulation found the orthorhombic $Ccca$ (No. 68) structure with 20 atoms in the conventional cell [as shown in Fig. 2(a)] has the lowest enthalpy. Its lattice parameters at 120 GPa are $a = 7.8518\,\text{Å}$, $b = 6.4520\,\text{Å}$, $c = 4.4536\,\text{Å}$. In this structure, there are two sets of atomic sites, one in the general Wyckoff position 16i sites at (0.1435, 0.6427, 0.1288) and the other in the special Wyckoff position 4a sites at the origin (0, 0, 0). The atoms in the 16i sites build the close-packed layer based on distorted hexagons [Fig. 2(e)], in which 2/3 of Sc-Sc intralayer distances are 2.55 Å and the remaining 1/3 are 2.12 Å. The 4a sites are occupied by the intercalated atoms between the adjacent distorted-hexagon layers (atoms marked in red in Fig. 2). In the conventional unit cell, each distorted-hexagon layer contains four atoms (denoted as layer A) in a close-packed manner, while each intercalated layer contains two atoms (denoted as layer B) in a loose-packed manner. They are arranged periodically along the crystallographic a axis, and we call this stacking sequence 2A+1B+2A+1B. It should be noted that such an assignment of layered motifs is based on the local atomic environment and Wyckoff symmetry. In fact, $Ccca$ is a very dense structure, and the "interlayer" separations (1.96 Å) are shorter than the "intralayer" separations (2.12 Å). Therefore, $Ccca$ and other structures that will be discussed in the following are not truly layered structures.

At pressures between 150 and 180 GPa, there exist two energetically competitive orthorhombic structures, i.e., the
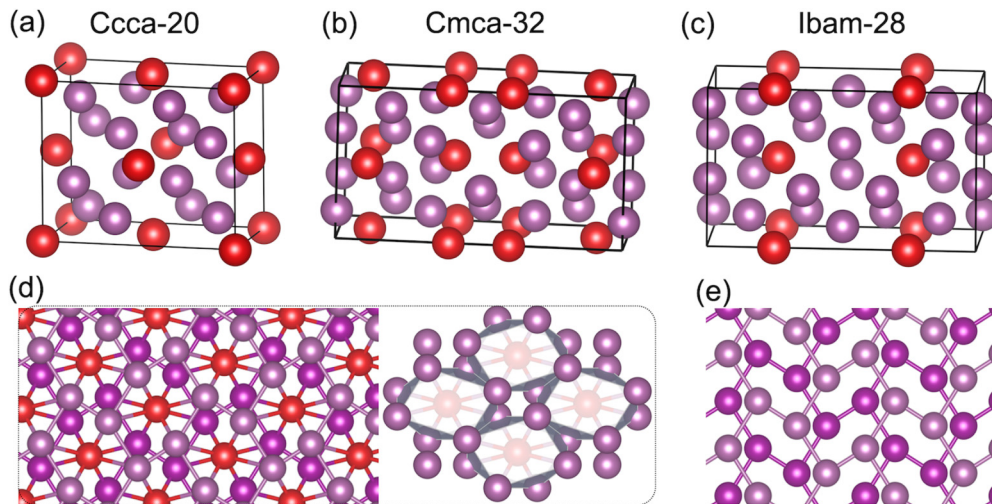
FIG. 2. The atomic structures of (a) *Ccca*-20, (b) *Cmca*-32, and (c) *Ibam*-28. (d) The model with the distorted-hexagon layer with intercalated atoms (left) and its polyhedron representation (right). (e) The hexagon layers without intercalated atoms. The atoms belonging to the distorted hexagon framework are denoted by purple spheres, while the intercalated atoms are denoted by red spheres.

Cmca (No. 64) structure with 32 atoms per unit cell and the *Ibam* (No. 72) structure with 28 atoms per unit cell [as shown in Figs. 2(b) and 2(c)]. *Cmca*-32 is the stablest structure when pressure is higher than 160 GPa. The lattice parameters at 150 GPa are $a = 12.2825$ Å, $b = 6.1338$ Å, $c = 4.4015$ Å. This structure has three different Wyckoff sites, 16g (0.8184, 0.1434, 0.8747), 8f (0.0000, 0.6609, 0.3900), and 8d (0.8961, 0.0000, 0.5000). Similar to *Ccca*-20, the Sc atoms at the 16g and 8f sites build the distorted-hexagon layered framework, while Sc atoms at 8d sites form the intercalated layers. *Ibam*-28 is marginally stable at 100–180 GPa, with the lattice parameters $a = 4.3916$ Å, $b = 6.3096$ Å, $c = 10.5340$ Å at 150 GPa, and atoms occupy 16k (0.3691, 0.1517, 0.8529), 8j (0.1702, 0.8809, 0.0000), and 4a sites (0.5000, 0.5000, 0.2500). Comparing these two structures, they both contain six close-packed distorted-hexagon layers. The difference lies in that intercalated atoms run every three hexagon layers in *Ibam*-28 (denoted as 3A+1B+3A+1B), while in *Cmca*-32 the intercalated atoms appear in every two and one hexagon layers (denoted as 2A+1B+1A+1B). More

interestingly, several energetically degenerate and geometrically similar structures can be constructed by changing the stacking sequence between A and B layers. As we will discuss in the following section, this phenomenon will lead to an infinite number of series of Sc allotropes. We also performed phonon calculations for all three structures proposed in this work at different pressure conditions. The absence of imaginary frequencies in the phonon spectrum [52] confirms that they are all dynamically stable.

At 250 GPa, we found several structures based on the stacking of hexagon layers, while the intercalated layers disappear. The energetics of those structures are extremely close (~ 2 meV/atom), within the numerical error of DFT calculation. In the range of 200–290 GPa, the stablest structure is the P-1 structure [Figs. 3(a) and 3(b)], while the experimentally identified $P6_122$ [37] is 3 meV/atom less stable than the P-1 structure at 250 GPa. The P-1 lattice parameters at 250 GPa are $a = 2.3367$ Å, $b = 7.1401$ Å, $c = 2.3389$ Å, $\alpha = 94.33°$, $\beta = 119.86°$, and $\gamma = 80.69°$. There are four atoms in the unit cell, with two types of general Wyckoff positions at (0.4341, 0.6251, 0.2501) and (0.1911, 0.1248, 0.7506). Given that these two structures possess extremely different PXRD patterns (see Fig. S7 in the Supplemental Material [52]), it is unlikely that the P-1 structure was present in the experiment [37]. We also calculated their free energy as a function of temperature based on harmonic phonon approximation. Surprisingly, it was found that the P-1 structure gained an even slightly enhanced stability (7 meV/atom at 300 K) relative to the $P6_122$ structure. Such a discrepancy may be due to strong anharmonic effects or the inadequacy of the pseudopotential used in the VASP code. However, an in depth study of this problem is beyond the scope of our current work.

We further plotted the enthalpies for all relevant structures as a function of pressure in Figs. 4 and S3 [52]. The ambient hcp phase remains stable up to 23 GPa, followed by the $I4/mcm(00\gamma)$ IC between 23 and 75 GPa, which is in excellent agreement with the experimental results [37], while the *Ccca*-20 structure is calculated to be the stablest phase at pressure higher than 75 GPa. However, in experiment, both
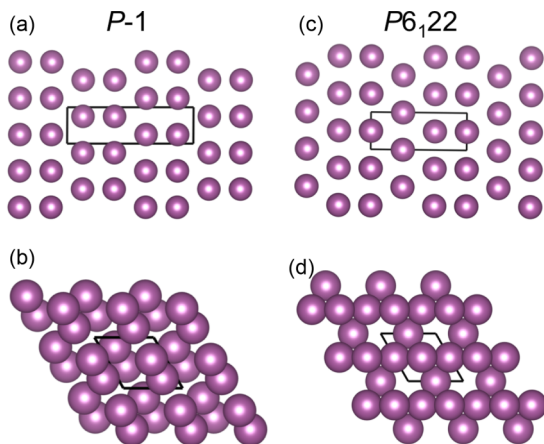

FIG. 3. The atomic structures of P-1, (a) side view and (b) top view, and $P6_122$, (c) side view and (d) top view.
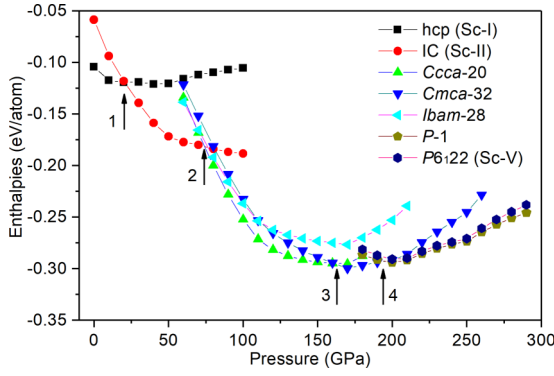
FIG. 4. Enthalpies of the hcp, IC, $Ccca$-20, $Cmca$-32, $Ibam$-28, P-1, and $P6_122$ structures (relative to the bcc structure). The arrows indicate the four phase transition points.

Akahama *et al.* [37] and Debessai *et al.* [18] reported that the host-guest structure transits to Sc-III at about 104–107 GPa. This may be due to the fact that we considered only the $I4/mcm$ structure as the candidate model for Sc-II. It was reported that under compression the incommensurate ratio γ between the host lattice ($c1$) and the guest lattice ($c2$) undergoes a significant variation from 1.28 to 1.36 [36,41]. Since this is not our focus, we do not include the modulation effects in our calculation. The $Cmca$-32 structure becomes the stablest at 160 GPa, while $Ibam$-28 is energetically close in the entire pressure range studied in this work. Above 195 GPa, the hexagonal close-layer-packing P-1 structure has the lowest enthalpy. We note that in experiment the Sc-IV to Sc-V transition takes place at about 240 GPa, but our
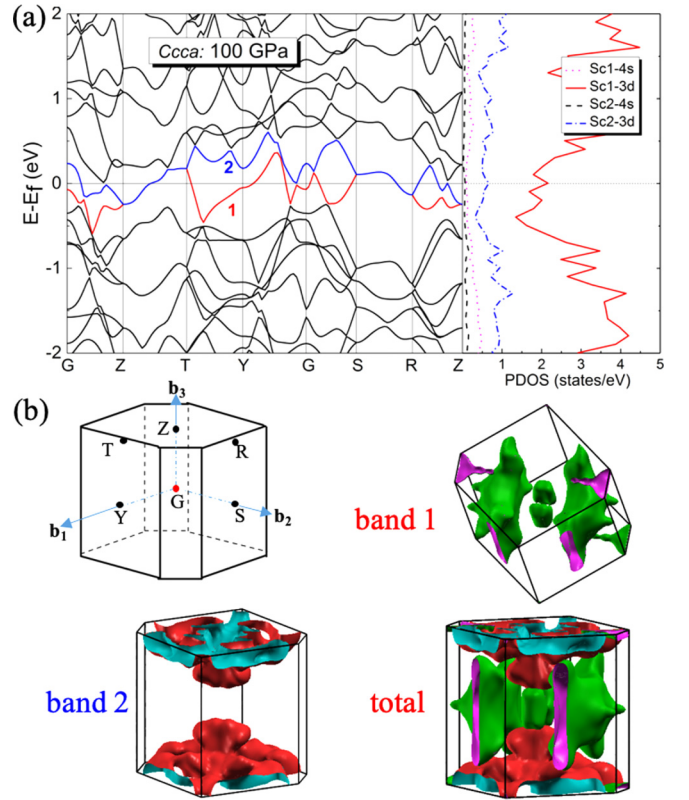

FIG. 5. (a) The electronic band structure along high-symmetry lines of the Brillouin zone and projected DOS and the Fermi surface of Sc in the $Ccca$ phase calculated at 100 GPa. The energy bands crossing the Fermi level are labeled 1 and 2, respectively.
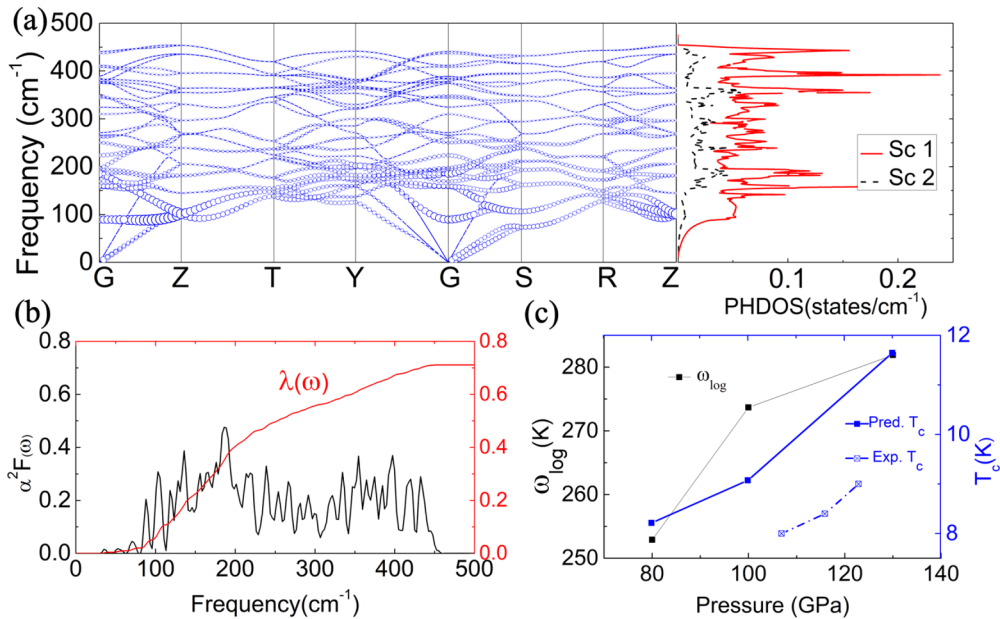

FIG. 6. (a) Phonon dispersion along the high-symmetry directions of the Brillouin zone (left panel) and the partial phonon density of states (PHDOS; right panel) of the $Ccca$-Sc at 100 GPa. Blue circles in the phonon dispersion show the EPC with a radius proportional to the respective coupling strength. (b) The Eliashberg phonon spectral function and the integrated EPC parameter λ as a function of frequency. (c) The superconducting transition temperature T_c and ω_{log} as a function of pressure, where the solid blue curve is from calculation, and the dash-dotted blue curve is from experiment data in Ref. [18].

prediction is 195 GPa. As discussed above, the discrepancy may be due to kinetic reasons, the anharmonic effect, or the limit of pseudopotential used in this study. Nevertheless, the prediction phase transition sequence in our study is, overall, in qualitative agreement with the experiment [37].

B. Superconductivity of *Ccca*-20

The superconducting behaviors for transition metals have been widely studied in the past. Unlike the simple *s* metals, the T_c of transition metals usually shows a highly nonlinear dependence as a function of pressure. Such complexity is attributed to the nature of *d* electrons and also structural transitions under pressure [18]. As the first member in this group, the T_c pressure dependence of Sc has been studied by several groups [18,20,21,42]. Debessai *et al.* found that the T_c in scandium reached the highest value of 19.7 K at 107 GPa and then dropped to about 8 K under further compression to 123 GPa [18]. The sudden decrease of T_c above 107 GPa is consistent with the phase transition pressure ($\sim$104 GPa) found by McMahon *et al.* using the monochromatic synchrotron PXRD [35]. In the past, an in-depth study of the superconducting behavior of Sc-III was prohibited due to the lack of a structural model. Herein, we chose the most likely *Ccca*-20 as the model structure to explore its superconducting properties. We calculated its electronic band structure, density of states (DOS), phonon spectra, and the Fermi surface at three different pressures, 80, 100, and 130 GPa.

We found that the electronic band structure of *Ccca*-20 does not notably change in the investigated pressure range. Figure 5 shows a typical picture at 100 GPa. The band structure reveals metallic character with large dispersion bands crossing the Fermi level E_{Fermi}. From Fig. 5(a), it is clear that only two bands are partially occupied in the band structure, i.e., two bands across the Fermi level, referred to as band 1 and band 2. For the *Ccca*-20 phase, the G point holds the D_{2h} point group. At the G point, these two bands across the Fermi level hold B_{2g} and A_g symmetry, respectively. The energy bands crossing the Fermi level are depicted in Fig. 5(b). The lower band (band 1) in energy gives an electronlike Fermi pocket around the G point. In addition, two quasiparallel pieces of Fermi sheets plot in the Fermi surface present an obvious Fermi nesting characteristic, signaling strong electron-phonon coupling. The Fermi surface originating from band 2 shows an electronlike characteristic around high-symmetry points Z and R in the Brillouin zone. The DOS near the Fermi level is mainly contributed by Sc 3*d* electrons, while Sc 4*s* electrons make a relatively smaller contribution to the electronic properties of *Ccca*-20.

To investigate the possible superconductivity on *Ccca*-20, we also computed its EPC parameter λ and the Eliashberg phonon spectral function $\alpha^2 F(\omega)$. The phonon band structure and the projected DOS at 100 GPa are shown in Fig. 6(a). The absence of imaginary frequency modes indicates its dynamic stability. Additional phonon calculations establish the stability range to be between 80 and 130 GPa. To quantify the contribution of each phonon branch, we decompose the EPC strength of each *q* point λ_q along the high-symmetry points in the BZ. The sizes of the blue circles in Fig. 6(a) indicate their relative contribution to the total λ. Clearly, we found
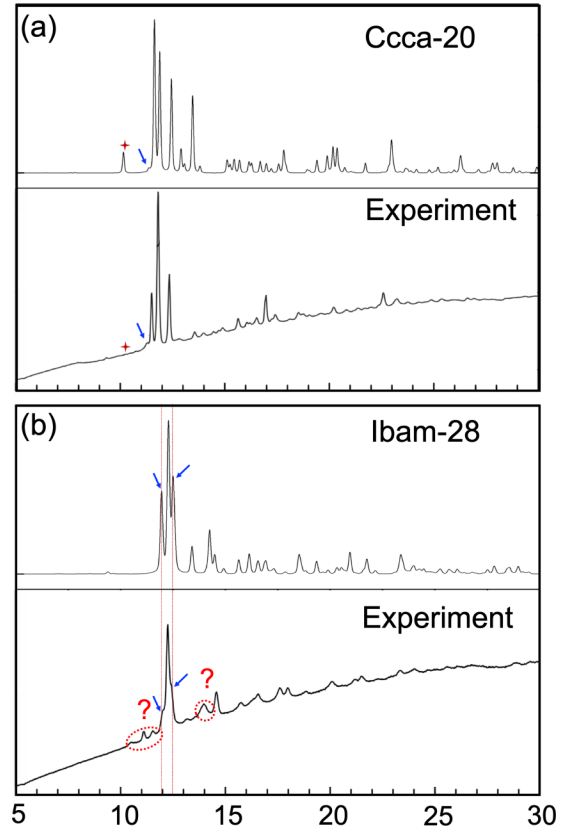

FIG. 7. Summary of the PXRD comparison between the predicted structures and experiment with a wavelength λ of 0.4428 Å. (a) *Ccca*-20 and Sc-III from experiment [37]; (b) *Ibam*-28 and Sc-IV from experiment. In general, there is qualitative agreement between experiment and prediction in terms of the first few strongest peaks. However, the predicted structures exhibit more reflection peaks in the high-angle range.

that the phonons below 240 cm^{-1} contribute significantly to λ [see also Fig. 6(b)]. In particular, the fourth and seventh phonon branches make the largest contributions. By analyzing their eigenvectors, we found that they are associated with the B_{1u} and B_{3g} vibrational modes. The spectral function $\alpha^2 F(\omega)$ obtained at 100 GPa and the integrated λ as a function of frequency are depicted in Fig. 6(b). The results suggest that the majority rise of λ is in the frequency region between 80 and 240 cm^{-1}, which is consistent with our phonon band analysis. The calculated λ is 0.710 at 100 GPa, in which the acoustic modes below 300 cm^{-1} constitute 78.6% of the total λ, while the higher vibrational modes contribute only 21.4%. This result is comparable to the previous studies on other close systems [53].

To obtain a rough estimation of the superconducting transition temperature T_c, we adopted the modified formula by Allen and Dynes [54],

$$T_c = \frac{\omega_{\log}}{1.2} \exp\left[-\frac{1.04(1+\lambda)}{\lambda - \mu^*(1+0.62\lambda)}\right], \quad (1)$$

where $\omega_{\log}$ can be calculated directly from the phonon spectrum as follows:

$$\omega_{\log} = \exp\left[\frac{2}{\lambda}\int_0^\infty \frac{d\omega}{\omega}\alpha^2 F(\omega)\ln\omega\right]. \quad (2)$$
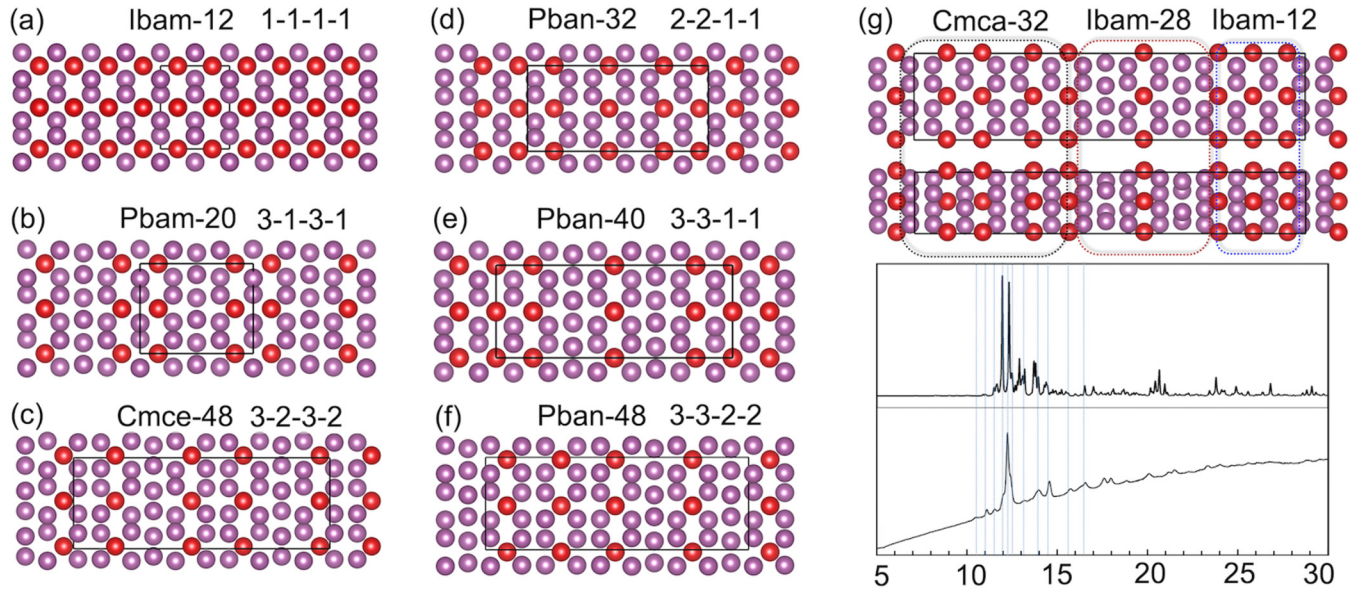
FIG. 8. The atomic structures of (a) *Ibam*-12 (1-1-1-1), (b) *Pbam*-20 (3-1-3-1), (c) *Cmce*-48 (3-2-3-2), (d) *Pbam*-32 (2-2-1-1), (e) *Pban*-40 (3-3-1-1), and (f) *Pban*-48 (3-3-2-2). (g) Top: The atomic structure of a supercell containing different fragments from *Cmca*-32, *Ibam*-28, and *Ibam*-12. Bottom: The PXRD profiles between simulation and experiment. The low-angle peaks from the supercell structure match well with those from experiment. The Sc atoms in the layer framework are denoted by purple spheres, and Sc atoms in the intercalated layer are denoted by red spheres.

In Eq. (1), μ^* is the Coulomb pseudopotential, which is usually between 0.10 and 0.13 for most metals [55]. At 100 GPa, the calculated $\omega_{\log}$ is 274 K. When $\mu^* = 0.11$, the estimated T_c is about 9.0 K. To study the pressure dependence of T_c, we also performed the EPC calculations at 80 and 130 GPa. The calculated $\omega_{\log}(\lambda)$ at 80, 100, and 130 GPa are 253 K (0.704), 274 K (0.710), and 282 K (0.779), respectively. T_c of *Ccca*-20 shows a monotonic increase with pressure, from 8.2 K at 80 GPa to 9.0 K at 100 GPa and 11.6 K at 130 GPa. In experiment, the corresponding T_c values were found to be 8 K at 107 GPa and 9 K at 123 GPa [18]. We can see that both the tendency and the T_c values are in satisfactory agreement with the experimental data, which supports that the *Ccca*-20 structure is likely to be the experimentally observed Sc-III.

C. PXRD comparison with the previous experimental results

In addition to the T_c measurements, another set of available experimental data for Sc-III/IV is the PXRD pattern. Therefore, we also compared the low-energy structures with the unsolved experimental Sc-III/IV in terms of the PXRD profiles (see Fig. 7). From Fig. 7(a), we found the simulated PXRD of the *Ccca*-20 structure has a strong similarity to the experimental Sc-III. In particular, both structures have the strongest three peaks at 11.63°, 11.88°, and 12.42° ($\lambda = 0.4428$ Å) at 115 GPa. Another weak peak at 11.36°, shown by a blue arrow in Fig. 7(b), was regarded as the impurity of the sample by Akahama *et al.* [37]. But our results suggest that this belongs to an intrinsic reflection peak of *Ccca*-20. Regardless of the qualitative agreement in the peak positions, we fail to find a plausible match in the peak intensities. This may be due to the possible texturing of the samples used in experiment or contamination from the secondary phase. Although it is insufficient to conclude that *Ccca*-20

is the right model for Sc-III, we suggest that *Ccca*-20 is a possible candidate model based on the fair match in PXRD, its energetic stability, and the superconductivity trend in the corresponding pressure range.

At higher pressure, our prediction suggested that *Cmca*-32 is the stablest. However, the simulated PXRD of *Cmca*-32 is extremely different from Sc-IV, as observed in experiment [37] (see Fig. S4 [52]). Another metastable structure, *Ibam*-28, seems to provide a better fit to Sc-IV. As shown in Fig. 7(b), the experiment PXRD profile has three main peaks, namely, two shoulder peaks and one main peak, which match those in *Ibam*-28 fairly well in terms of both peak position and intensity. It is reasonable to speculate that *Ibam*-28 may, at least partially, explain the observed pattern for Sc-IV. Given that *Ibam*-28 is marginally less stable than *Cmca*-32, it is kinetically indeed possible that it exists in experiment.

Yet there are still some weak peaks missing in the simulated PXRD, especially in the low-degree region [see the dotted circles in Fig. 7(b)]. The extra peaks of the experimental PXRD indicate Sc-IV may be a mixture of different structures. Here, we manually constructed a series of structures with different stacking sequences of A and B layers and then optimized their geometries at 150 GPa by DFT. Figure 8 shows these structures (their enthalpy-pressure relations can be found in Fig. S5 [52]). Based on our earlier descriptions of *Ccca*-20 (2A+1B+2A+1B), *Ibam*-28 (3A+1B+3A+1B), and *Cmca*-32 (2A+1B+1A+1B), we name them 2-2-2-2, 3-3-3-3, and 2-1-2-1, respectively. Here, the digit number corresponds to the number of A layers, and the transverse means the connecting B layer. Following the same convention, we name these trial structures as follows: *Ibam*-12 (1-1-1-1), *Pbam*-20 (3-1-3-1), *Cmce*-48 (3-2-3-2), *Pban*-32 (2-2-1-1), *Pban*-40 (3-3-1-1), *Pban*-48 (3-3-2-2), and so on. The simulated PXRD profiles of those structures are shown in Fig. S6 [52].

Comparing with experiment data, we find that the structures with "-1-1" termination indeed exhibit the low-angle weak-reflection peaks consistent with the experimental pattern. This suggests that the Sc-IV phase may contain a small portion of other structures like $Ibam$-12 or similar structures. To confirm this hypothesis, we constructed a supercell structure which contains $Cmca$-32, $Ibam$-28, and $Ibam$-12 local structure; as shown in Fig. 8(g), the simulated PXRD can indeed match the experiment one well in the entire 2θ range. Although still speculative, this suggests that the real structure may be described by the structural unit model which has been used to describe the material grain boundary [56].

Fermi pocket around the Γ point and two quasiparallel pieces of Fermi sheets plot in the Fermi surface. Our calculation also suggested that the strong EPC is mainly contributed by the low-frequency phonon modes. For the high-pressure form of Sc-IV, we failed to find any single structure that can match the observed PXRD pattern well. Instead, a model based on random stacking of two different building blocks seems to yield the best agreement with the experimental PXRD. This suggests that Sc at high pressure may adopt a complex structure by assembling different structural units. Although the current results are insufficient to fully determine the crystal structures of Sc-III/IV, we hope the proposed models here can serve as a guide for following studies in the future.

IV. CONCLUSION

In conclusion, using the *ab initio* evolutionary structure prediction method USPEX, we performed a thorough crystal structure search to explore the high-pressure phases of Sc. We reported the $Ccca$-20 structure as a possible candidate for the high-pressure allotropes of Sc-III. This is supported by the fair agreements in both the PXRD pattern and superconducting properties between experiment and prediction. Using $Ccca$-20 as the model system, we observed a typical Fermi nesting characteristic as indicated by two partial occupied energy bands across the Fermi level exhibiting an electronlike

ACKNOWLEDGMENTS

[1] M. I. McMahon and R. J. Nelmes, Chem. Soc. Rev. **35**, 943 (2006).

[2] P. W. Bridgman, General Outlook on the Field of High-pressure Research, in *Collected Experimental Papers*, Vol. VII Papers 169–199 (Harvard University Press, 1964), pp. 4625–4638.

[3] S. Jiang, H. Wang, Y. Wu, X. Liu, H. Chen, M. Yao, B. Gault, D. Ponge, D. Raabe, A. Hirata *et al.*, Nature (London) **544**, 460 (2017).

[4] L. Lu, Y. Shen, X. Chen, L. Qian, and K. Lu, Science **304**, 422 (2004).

[5] R. Wang and M. D. Merz, Nature (London) **260**, 35 (1976).

[6] D. A. Young, *Phase Diagrams of the Elements* (University of California Press, 1991).

[7] O. Degtyareva, M. I. McMahon, D. R. Allan, and R. J. Nelmes, Phys. Rev. Lett. **93**, 205502 (2004).

[8] S. Arapan, H.-k. Mao, and R. Ahuja, Proc. Natl. Acad. Sci. USA **105**, 20627 (2008).

[9] M. Hanfland, K. Syassen, N. Christensen, and D. Novikov, Nature (London) **408**, 174 (2000).

[10] J. Lv, Y. Wang, L. Zhu, and Y. Ma, Phys. Rev. Lett. **106**, 015503 (2011).

[11] T. Matsuoka and K. Shimizu, Nature (London) **458**, 186 (2009).

[12] V. V. Struzhkin, M. I. Eremets, W. Gan, H.-k. Mao, and R. J. Hemley, Science **298**, 1213 (2002).

[13] M. Marqués, M. I. McMahon, E. Gregoryanz, M. Hanfland, C. L. Guillaume, C. J. Pickard, G. J. Ackland, and R. J. Nelmes, Phys. Rev. Lett. **106**, 095502 (2011).

[14] Y. Ma, M. Eremets, A. R. Oganov, Y. Xie, I. Trojan, S. Medvedev, A. O. Lyakhov, M. Valle, and V. Prakapenka, Nature (London) **458**, 182 (2009).

[15] E. Gregoryanz, L. F. Lundegaard, M. I. McMahon, C. Guillaume, R. J. Nelmes, and M. Mezouar, Science **320**, 1054 (2008).

[16] M. McMahon, E. Gregoryanz, L. Lundegaard, I. Loa, C. Guillaume, R. Nelmes, A. Kleppe, M. Amboage, H. Wilhelm, and A. Jephcoat, Proc. Natl. Acad. Sci. USA **104**, 17297 (2007).

[17] B. Rousseau, Y. Xie, Y. Ma, and A. Bergara, Eur. Phys. J. B **81**, 1 (2011).

[18] M. Debessai, J. J. Hamlin, and J. S. Schilling, Phys. Rev. B **78**, 064519 (2008).

[19] A. Ormeci, K. Koepernik, and H. Rosner, Phys. Rev. B **74**, 104119 (2006).

[20] S. Bose, J. Phys. Condens. Matter **20**, 045209 (2008).

[21] B. Kong, L. Zhang, X.-R. Chen, T.-X. Zeng, Z.-Y. Zeng, and L.-C. Cai, Solid State Commun. **151**, 1972 (2011).

[22] W. Grosshans, Y. Vohra, and W. Holzapfel, J. Magn. Magn. Mater. **29**, 282 (1982).

[23] G. K. Samudrala, G. M. Tsoi, and Y. K. Vohra, J. Phys. Condens. Matter **24**, 362201 (2012).

[24] G. N. Chesnut and Y. K. Vohra, Phys. Rev. Lett. **82**, 1712 (1999).

[25] H. Olijnyk, W. A. Grosshans, and A. P. Jephcoat, Phys. Rev. Lett. **93**, 255505 (2004).

[26] G. K. Samudrala, S. A. Thomas, J. M. Montgomery, and Y. K. Vohra, J. Phys. Condens. Matter **23**, 315701 (2011).

[27] W. Zeng, V. Heine, and O. Jepsen, J. Phys. Condens. Matter **9**, 3489 (1997).

[28] H. L. Skriver, Phys. Rev. B **31**, 1909 (1985).

[29] N. V. Morozova, V. V. Shchennikov, and S. V. Ovsyannikov, J. Appl. Phys. **118**, 225901 (2015).

[30] M. Debessai, T. Matsuoka, J. J. Hamlin, J. S. Schilling, and K. Shimizu, Phys. Rev. Lett. **102**, 197002 (2009).

[31] B. Johansson and A. Rosengren, Phys. Rev. B **11**, 2836 (1975).

[32] L. W. Nixon, D. Papaconstantopoulos, and M. J. Mehl, Phys. Rev. B **76**, 134512 (2007).

[33] Y. K. Vohra, W. Grosshans, and W. B. Holzapfel, Phys. Rev. B **25**, 6019 (1982).

[34] H. Olijnyk, S. Nakano, A. Jephcoat, and K. Takemura, J. Phys. Condens. Matter **18**, 10971 (2006).

[35] M. I. McMahon, L. F. Lundegaard, C. Hejny, S. Falconi, and R. J. Nelmes, Phys. Rev. B **73**, 134102 (2006).

[36] H. Fujihisa, Y. Akahama, H. Kawamura, Y. Gotoh, H. Yamawaki, M. Sakashita, S. Takeya, and K. Honda, Phys. Rev. B **72**, 132103 (2005).

[37] Y. Akahama, H. Fujihisa, and H. Kawamura, Phys. Rev. Lett. **94**, 195503 (2005).

[38] M. McMahon and R. Nelmes, Z. Kristallogr.-Cryst. Mater. **219**, 742 (2004).

[39] A. M. Molodets, D. V. Shakhray, A. A. Golyshev, and V. E. Fortov, Phys. Rev. B **75**, 224111 (2007).

[40] R. Briggs, M. Gorman, A. Coleman, R. McWilliams, E. McBride, D. McGonegle, J. Wark, L. Peacock, S. Rothman, S. Macleod *et al.*, Phys. Rev. Lett. **118**, 025501 (2017).

[41] S. Arapan, N. V. Skorodumova, and R. Ahuja, Phys. Rev. Lett. **102**, 085701 (2009).

[42] J. Wittig, C. Probst, F. A. Schmidt, and K. A. Gschneidner, Jr., Phys. Rev. Lett. **42**, 469 (1979).

[43] J. J. Hamlin and J. S. Schilling, Phys. Rev. B **76**, 012505 (2007).

[44] Y. C. Zhao, F. Porsch, and W. B. Holzapfel, Phys. Rev. B **54**, 9715 (1996).

[45] S. Riva, K. V. Yusenko, N. P. Lavery, D. J. Jarvis, and S. G. Brown, Int. Mater. Rev. **61**, 203 (2016).

[46] A. R. Oganov and C. W. Glass, J. Chem. Phys. **124**, 244704 (2006).

[47] A. O. Lyakhov, A. R. Oganov, H. T. Stokes, and Q. Zhu, Comput. Phys. Commun. **184**, 1172 (2013).

[48] G. Kresse and J. Furthmüller, Phys. Rev. B **54**, 11169 (1996).

[49] J. P. Perdew, K. Burke, and M. Ernzerhof, Phys. Rev. Lett. **77**, 3865 (1996).

[50] A. Togo, F. Oba, and I. Tanaka, Phys. Rev. B **78**, 134106 (2008).

[51] P. Giannozzi, S. Baroni, N. Bonini, M. Calandra, R. Car, C. Cavazzoni, D. Ceresoli, G. L. Chiarotti, M. Cococcioni, I. Dabo *et al.*, J. Phys. Condens. Matter **21**, 395502 (2009).

[52] See Supplemental Material at http://link.aps.org/supplemental/10.1103/PhysRevB.98.214116 for a detailed description of the crystal structures, energetics. and x-ray diffraction pattern comparisons.

[53] Y. Chen, Q.-M. Hu, and R. Yang, Phys. Rev. Lett. **109**, 157004 (2012).

[54] P. B. Allen and R. Dynes, Phys. Rev. B **12**, 905 (1975).

[55] W. McMillan, Phys. Rev. **167**, 331 (1968).

[56] A. Sutton, Philos. Mag. Lett. **59**, 53 (1989).